Feedback Control of a Dielectric-Elastomer Soft Robot Using Modified Dubins Path Planning

Xinlei Li and Dong Wang

***Abstract*—Soft robots demonstrate enhanced safety and adaptability in complex and dynamic environments compared to rigid robots. Their unique actuation mechanisms, materials, structural designs, and environmental interactions necessitate distinct path planning methods. In this work, we develop a modified Dubins path planning method for a dielectric elastomer (DE) soft robot, integrating vision-based feedback control. Due to its structural design, the soft robot exhibits instantaneous forward, backward, and right-turn motions under different frequencies with a single voltage input. The modified Dubins path planning method accounts for these three distinct locomotion modes, providing optimal three- and two-segment paths. Image-based visual servoing enables real-time adjustments of the optimal path, enhancing adaptability under external disturbances. Experiments demonstrate that the soft robots can be controlled to reach targets from different initial orientations, navigate mazes, and achieve destinations despite wind disturbances.**

***Index Terms*—Dielectric elastomer (DE) actuation, feedback control, locomotion path planning, soft robotics.**

I. Introduction

SOFT robots are constructed from soft and flexible materials [1], [2], [3], [4], [5]. Due to the inherent compliance of soft materials, soft robots exhibit enhanced adaptability when navigating in complex, dynamic and unstructured environments. Various motion control methods have been proposed for soft robots with different actuation mechanisms and structural designs. Pneumatic soft robots, known for their lightweight, safe, low-cost, and easy fabrication, have been controlled using pneumatic circuits and viscous flow [6], [7]. Theoretical models have also been developed to achieve more accurate motions for fiber-reinforced [8], pneu-net [9], kirigami-inspired [10], and lattice-reinforced pneumatic soft manipulators [11]. However, the viscosity of the fluid and the need for an additional inflation pump hinders its response speed and miniaturization. Magnetic soft robots exhibit multimodal motions by manipulating external magnetic fields, but large magnetic field generators are required [12], [13], [14], [15], [16]. Electric actuations have the advantage of precise control, fast response and the possible ability of seamless integration with sensors and control circuitry, facilitating the design of autonomous soft robots [17], [18], [19], [20], [21], [22], [23], [24]. For example, a soft robot that forms an "8" path using three dielectric-elastomer (DE) actuators is developed by controlling the actuation sequences [18]. Ren et al. have designed a centipede-like soft robot and accomplished desired movement tasks using a neuro-inspired hierarchical motion control scheme [24].

TABLE I
Lists of Path Planning of Soft Robots

Robot Types	Actuation Types	Path planning algorithm
Soft Manipulator [25]	Pneumatic	Weighted Jacobian Rapidly-exploring Random Tree
Soft Manipulator [28]	Pneumatic	Improved particle swarm optimization algorithm
Soft Manipulator [26]	Pneumatic	Whole Arm Planner
Soft Manipulator [27]	Cable-driven	Constrained motion planning
Soft Manipulator [29]	-	Efficient obstacle-aware algorithm
Morphing Soft Robots [30]	-	3D Voronoi diagrams and Dijkstra's algorithm
Soft robotic arms [31]	Electric	Statistics machine-learning algorithm
Soft Robotic Snake [32]	Pneumatic	Adaptive bounding box method

Despite extensive research on the motions of soft robots, path planning for soft robots remains in its infancy. Table I summarizes the path planning methods for soft robots. Most studies focus on pneumatic soft manipulators due to their versatility [25], [26], [27], [28], [29], [30]. For example, Liu et al. [28] developed an obstacle avoidance path planning method for soft robots using an improved particle swarm optimization algorithm. Fairchild et al. [29] used parametric equations for soft robotic arms navigating around multiple obstacles. Gough et al. [30] utilized 3-D Voronoi diagrams and Dijkstra's algorithm for morphing soft robots in congested environments. Path planning for electric-driven soft manipulators has also been studied. Wang et al. [31] developed a statistics machine-learning algorithm to plan the motion paths of soft robotic arms composed of

Manuscript received 27 May 2024; accepted 9 July 2024. Recommended by Technical Editor M. Rakotondrabe and Senior Editor M. Indri. This work was supported in part by the National Key Research and Development Program of China under Grant 2022YFB4700900, in part by the National Natural Science Foundation of China under Grant 52275025, in part by the State Key Laboratory of Mechanical System and Vibration under Grant MSVZD202301, and in part by the Chenguang Program of Shanghai Education Development Foundation and Shanghai Municipal Education Commission under Grant 19CG11. *(Corresponding author: Dong Wang.)*

Xinlei Li and Dong Wang are with the State Key Laboratory of Mechanical System and Vibration, School of Mechanical Engineering, Shanghai Jiao Tong University, Shanghai 200240, China, and also with Meta Robotics Institute, Shanghai Jiao Tong University, Shanghai 200240, China (e-mail: li_3238@sjtu.edu.cn; wang_dong@sjtu.edu.cn).

This article has supplementary material provided by the authors and color versions of one or more figures available at https://doi.org/10.1109/TMECH.2024.3427112.

Digital Object Identifier 10.1109/TMECH.2024.3427112

TABLE II
VARIOUS PATH PLANNING METHODS BASED ON THE DUBINS PATH

Vehicle Types	Dubins Path Type	Methods
UAV [33]	All types	Bezier-Dubins: Using Bezier-Dubins for path planning
Fixed Wing UAV [35]	All types	Three-dimensional Dubins path for airplane
Fixed Wing UAV [37]	All types	Lypaunov-based path-following control for search and rescue
UAV [39]	All types	Dijkstra to handling kinematic constraints and obstacles
UAV [40]	All types	3D Dubins curves with RRT to avoid obstacles
Fixed-Wing UAV [42]	All types	2D A* based on Dubins path
Nonholonomic AV [34]	All types	Reeds-Shepp curves numeric nonlinear optimization method
Nonholonomic AV [38]	All types	Hybrid A* planner with potential fields for Real-time planning and following
Nonholonomic AV [41]	All types	RRT for Real-time motion planning
Nonholonomic AV [43]	All types	Improved A* algorithm
Nonholonomic AV [44]	*RS, LS, RL, LR*	Path planning through a sequence of waypoints
Nonholonomic AV [45]	*RRR, LLL*	Time-optimal paths for Dubins vehicles with unidirectional turning constraints
This work	$RS^{+}R$, $RS^{-}R$	Modified Dubins path planning method for a DE soft robot

ionic-polymer-metal composites. However, locomotion path planning is relatively rare, as the locomotion requires the considerations of synergetic deformation and substrate contact. A notable study is the locomotion path planning of a modular soft robotic snake using the adaptive bounding box method [32].

In contrast, path planning for rigid robots has been extensively explored in applications such as, unmanned aerial vehicles (UAVs) and autonomous vehicles (AVs). Table II shows a list of the control strategies used. The Dubins path method has been adapted to deal with kinematic constraints. For example, Askari et al. [33] developed a path planning method for UAVs using the Bezier–Dubins curve for real-world missions requiring smooth transitions. Du et al. [34] developed an advanced heuristic graph search algorithm based on Dubins curves and nonlinear optimization. The 2-D Dubins path has been extended to 3-D space for UAVs [35]. Váňa et al. [36] developed a solution to find the shortest curvature-constrained path connecting two disk-shaped regions. Moreover, the Dubins method has also been combined with path-following strategies for efficient and precise control. For example, Lugo-Cárdenas et al. [37] developed a path generator for UAV, integrating Dubins paths and Lyapunov-based control for efficient search and rescue missions. Hemmat et al. [38] developed a real-time path planning and following method in unstructured environments based on Dubins path and pure-pursuit algorithm. Meanwhile, obstacle avoidance algorithms such as, Dijkstra [39], RRT [40], [41], and A* [42], [43] are frequently integrated with Dubins path for nonholonomic vehicles' navigation in complex environments.

Path planning algorithms for rigid robots cannot be directly applied to soft robots due to differences in actuation mechanisms, material use, structural design, and environmental interaction. Although the Dubins methods have been extensively explored to address various path planning problems, most studies explore all six possible motion combinations: RSR, RSL, LSL, LSR, RLR, and LRL [33], [34], [35], [36], [37], [38], [40], [41], [42], [43]. Some works focus only on a subset of these combinations, typically considering both right and left directions [44], [45]. Recently, a dexterous electric-driven soft robot was developed that exhibits instantaneous forward, backward, and right-turn motions under different frequencies with a single voltage input, which facilitates path planning using a single input [46]. However, the Dubins method considering the forward, backward, and right-turning motions has not been developed.

Soft robots are highly sensitive to environmental disturbance, which can severely undermine their accuracy and precision during locomotion. Image-based visual servoing (IBVS) has been extensively applied in robotics for tasks that require interaction with the physical world, such as, grasping objects, tracking moving targets, and navigating through environments [47]. Its application in soft robotics is receiving increased attention [48], [49]. For example, Xu et al. [48] developed a vision-based shape control scheme for a soft robot manipulator, enabling accurate shape control without 3-D position signals. Lazo et al. [49] designed a 3-D-printed endoscopic soft robot for intraluminal navigation, employing visual servoing with convolutional neural networks to autonomously and safely navigate hollow environments. Integrating path planning and feedback control is a promising way to realize stable locomotion.

In this work, we develop a locomotion path planning method for an electric-driven soft robot based on a modified Dubins path and IBVS control. The soft robot consists of a saddle-shape DE actuator, a chiral lattice, and a plate foot. Due to the bouncing behavior and the coupled compression-twisting effect of the chiral foot, it exhibits instantaneous forward, backward, and right turn motions under different frequencies with a single voltage input. Unlike the traditional Dubins path, which allows forward movement and left and right turns, the modified Dubins path planning method accounts for the soft robot's forward, backward, and right-turn motions. The there-segment path is further reduced to a two-segment path when the destination orientation is not restricted. IBVS is used to make real-time adjustments to the optimal path. Numerical stability analysis is conducted. Results demonstrate that the soft robots can be controlled to reach points from different initial orientations, navigate mazes, and reach destinations despite wind disturbances.

The main contribution of this work can be summarized as follows. 1) We developed a modified Dubins path method considering forward, backward, and right-turn motions. 2) We developed a control algorithm that uses IBVS for real-time adjustments of the optimal path. 3) We have implemented the path planning method into an electric-driven soft robot and demonstrated its capacity to reach points with different initial orientations, navigate mazes, and resist external disturbances.

II. STRUCTURAL DESIGN AND MOTIONS

The soft robot consists of a saddle-shape DE actuator, a chiral lattice and a plate foot [see Fig. 1(a)]. The DE actuator comprises a prestretched DE membrane and a flexible acrylic frame.

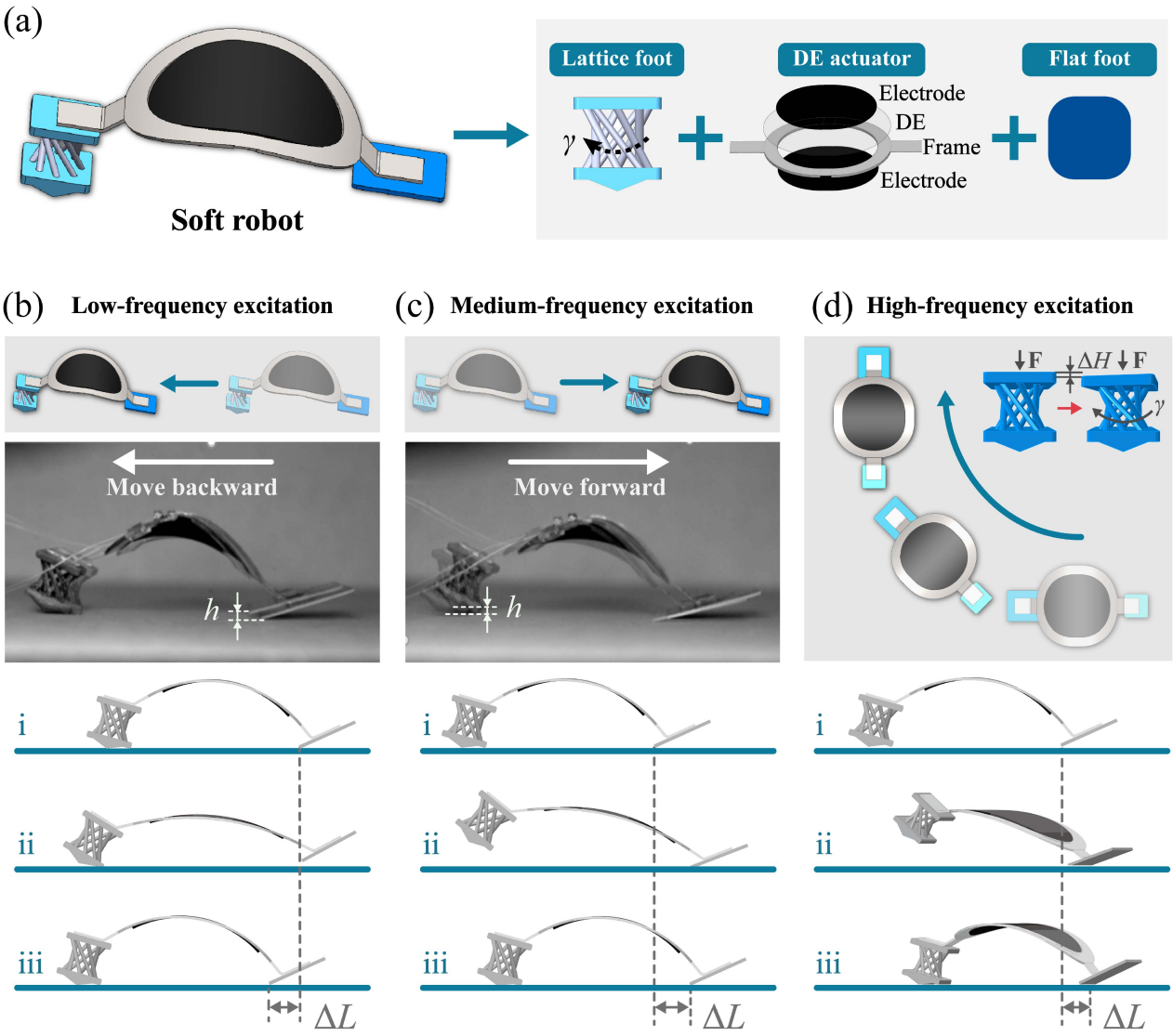

Fig. 1. Structural design and motions. (a) The soft robot comprises a saddle-shape DE actuator, a chiral lattice and a plate foot. (b) The soft robot moves backward at a relatively low frequency as the flat foot jumps above the ground. (c) The soft robot moves forward at a medium frequency as the chiral lattice foot bounces above the ground. (d) The soft robot moves in a circular direction at a high frequency due to the compression-twisting effect.

The DE membrane, biaxially prestretched 3.5 × 3.5 times, is sandwiched between two compliant carbon grease electrodes and adhered to the acrylic frame. Upon releasing the stretched membrane, the DE actuator buckles into a saddle-shaped structure. The DE layer can extend or contract repeatedly by applying sinusoidal voltage. The feet are fabricated by a commercial 3-D printer (Stratasys J750) with Vero material. The chiral lattice foot is composed of eight straight beams connected to the top and bottom plates, with a prism structure at the bottom plate to guide locomotion direction. All beams are twisted at an angle $\gamma = 90°$ counter-clockwise, resulting in a compression-twisting coupled effect.

Due to the structural design, the soft robots exhibit forward, backward, or turning motions under different frequencies. When a high-voltage input is applied, the DE actuator contracts and expands periodically. At relatively low frequencies, the soft robot's lattice foot remains on the ground while the flat foot jumps during contraction due to its lightweight. Consequently, the soft robots move toward the lattice foot [see Fig. 1(b)]. As the frequency increases, the lattice foot bounces above the ground due to the dynamic bouncing while the flat foot stays on the ground. Its locomotion direction reverses [see Fig. 1(c)]. When the applied frequency increases further to approach the natural frequency of the lattice foot, resonance causes a large compression between the plates, generating the compression-twisting effect. As a result, the lattice foot twists and the soft robot moves circularly [see Fig. 1(d)]. Movie 1 illustrates the operational mechanisms of the soft robots. The soft robot's movements were captured with a high-speed camera. Experiments show that the lattice foot remains on the ground at low frequencies but jumps at higher frequencies. Detailed theoretical, experimental and FE simulations of the operational mechanism of the soft robots have been illustrated in the previous work [46].

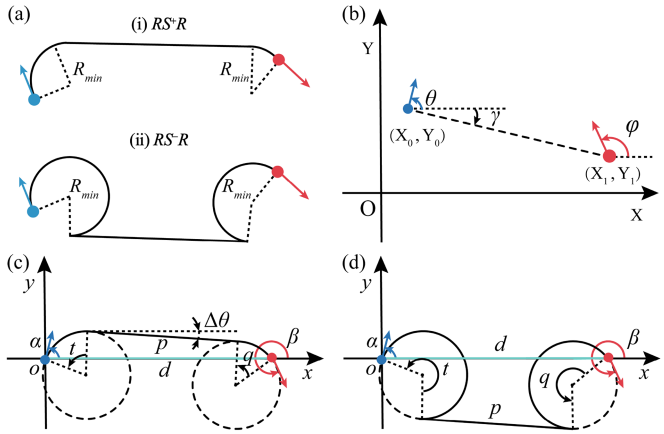

Fig. 2. Modified Dubins path. (a) The trajectories of the two types of paths: RS^+R and RS^-R. (b) The coordinates of the starting and target points. (c) RS^+R path and (d) RS^-R path in the normalized coordinate.

III. Path Planning Algorithm

Dubins path is a widely used algorithm to find the optimal path of two points when forward, left and right turning motions are allowed [50]. However, it cannot be directly applied to the developed soft robot, as it exhibits front, backward and turn right motions. The Dubins path algorithm is modified for the developed soft robot, and the three-segment optimal path is reduced to two segments to simplify the control.

A. Modified Dubins Path Planning

The Dubins path refers to the shortest path between two points in a 2-D space with a constraint on the curvature. Specifically, the Dubins path considers the object's ability to move forward only and restricts it from moving backward. The optimal path is represented by combinations of "right turn (R)," "left turn (L)," and "forward (S^+)" segments, which can be classified into six types: RS^+R, RS^+L, LS^+R, LS^+L, RLR, and LRL. Each type corresponds to a specific sequence of maneuvers that connect the initial and final positions. The right and left turns represent turning with the minimum curvature. The shortest path is the minimum of the six paths, stated as

$$\min\left[L_{RS^+R}, L_{RS^+L}, L_{LS^+R}, L_{LS^+L}, L_{RLR}, L_{LRL}\right]. \quad (1)$$

Since left turn is not allowed for the developed soft robot, only RS^+R type is selected

$$\begin{aligned}&\min\left[L_{RS^+R}, L_{RS^+L}, L_{LS^+R}, L_{LS^+L}, L_{RLR}, L_{LRL}\right]\\ &= \min[L_{RS^+R}]. \end{aligned} \quad (2)$$

Considering the soft robot can move backward, another possible path is L_{RS^-R}. Here, we use S^- denotes the backward motions. As

$$\min[L_{RS^+R}] \geq \min\left[L_{RS^+R}, L_{RS^-R}\right] \quad (3)$$

the minimum value of L_{RS^+R} and L_{RS^-R} is chosen as the optimal path. Fig. 2(a) shows the trajectories of both RS^+R and RS^-R paths.

B. Path Length Calculation

The coordinates of the starting and target points are set as $(\mathrm{X}_0, \mathrm{Y}_0, \theta)$ and $(\mathrm{X}_1, \mathrm{Y}_1, \varphi)$ [see Fig. 2(b)]. Here $(\mathrm{X}_0, \mathrm{Y}_0)$ and $(\mathrm{X}_1, \mathrm{Y}_1)$ denote the positions in the Cartesian coordinate. θ and φ present the initial and target orientations. The Cartesian coordinate is normalized by setting the x-axis along the line that connects the two points. The length is normalized by the minimum turning radius $R_{\min}$. The starting point is set as the origin. Fig. 2(c) and (d) shows the normalized RS^+R and RS^-R paths, respectively. The normalized distance d between the initial and target positions is

$$d = \frac{\sqrt{(\mathrm{Y}_1 - \mathrm{Y}_0)^2 + (\mathrm{X}_1 - \mathrm{X}_0)^2}}{R_{\min}}. \quad (4)$$

The orientations θ and φ become α and β, given by

$$\alpha = \theta - \gamma \quad \text{and} \quad \beta = \varphi - \gamma \quad (5)$$

where $\gamma = \arctan(\frac{\mathrm{Y}_1 - \mathrm{Y}_0}{\mathrm{X}_1 - \mathrm{X}_0})$. The normalized RS^+R path consists of two arcs and a tangent line connecting both circles [see Fig. 2(c)]. Its length $\tilde{L}_{RS^+R}$ is

$$\tilde{L}_{RS^+R} \equiv L_{RS^+R}/R_{\min} = t_{RS^+R} + q_{RS^+R} + p_{RS^+R} \quad (6)$$

where t_{RS^+R}, q_{RS^+R} and p_{RS^+R} are the normalized lengths of the two arcs and the tangent line, respectively. The length of the tangent line p_{RS^+R} is calculated as

$$p_{RS^+R} = \sqrt{2 + d^2 - 2\cos(\alpha - \beta) + 2d(\sin\beta - \sin\alpha)}. \quad (7)$$

The normalized lengths of the two arcs are

$$t_{RS^+R} = \mathrm{mod}\,(\alpha - \Delta\theta, 2\pi) \quad (8)$$

$$q_{RS^+R} = \mathrm{mod}\,(2\pi - \beta + \Delta\theta, 2\pi) \quad (9)$$

where $\Delta\theta$ is the angle between the tangent line and x-axis

$$\Delta\theta = \arctan\left(\frac{\cos\beta - \cos\alpha}{d + \sin\beta - \sin\alpha}\right). \quad (10)$$

Substituting (7)–(10) into (6), L_{RS^+R} can be obtained.

Fig. 2(d) shows the trajectory of path RS^-R. The normalized length of the two arcs and the tangent line for the path RS^-R are given as

$$t_{RS^-R} = \mathrm{mod}\,(\alpha - \pi - \Delta\theta, 2\pi) \quad (11)$$

$$q_{RS^-R} = \mathrm{mod}\,(\pi - \beta + \Delta\theta, 2\pi) \quad (12)$$

and

$$\begin{aligned} p_{RS^-R} &= p_{RS^+R}\\ &= \sqrt{2 + d^2 - 2\cos(\alpha - \beta) + 2d(\sin\beta - \sin\alpha)}. \end{aligned} \quad (13)$$

The length of path $\tilde{L}_{RS^-R}$ can then be obtained by

$$\tilde{L}_{RS^-R} \equiv L_{RS^-R}/R_{\min} = t_{RS^-R} + q_{RS^-R} + p_{RS^-R}. \quad (14)$$

The minimum value of L_{RS^+R} and L_{RS^-R} is then chosen as the optimal path for the electric-driven soft robot. Fig. 3(a) and (b) plots the dependence of $\tilde{L}_{RS^+R}$ and $\tilde{L}_{RS^-R}$ on the destination orientation β for $(\alpha, d) = (\pi/6, 10)$ and $(7\pi/6, 10)$, respectively.

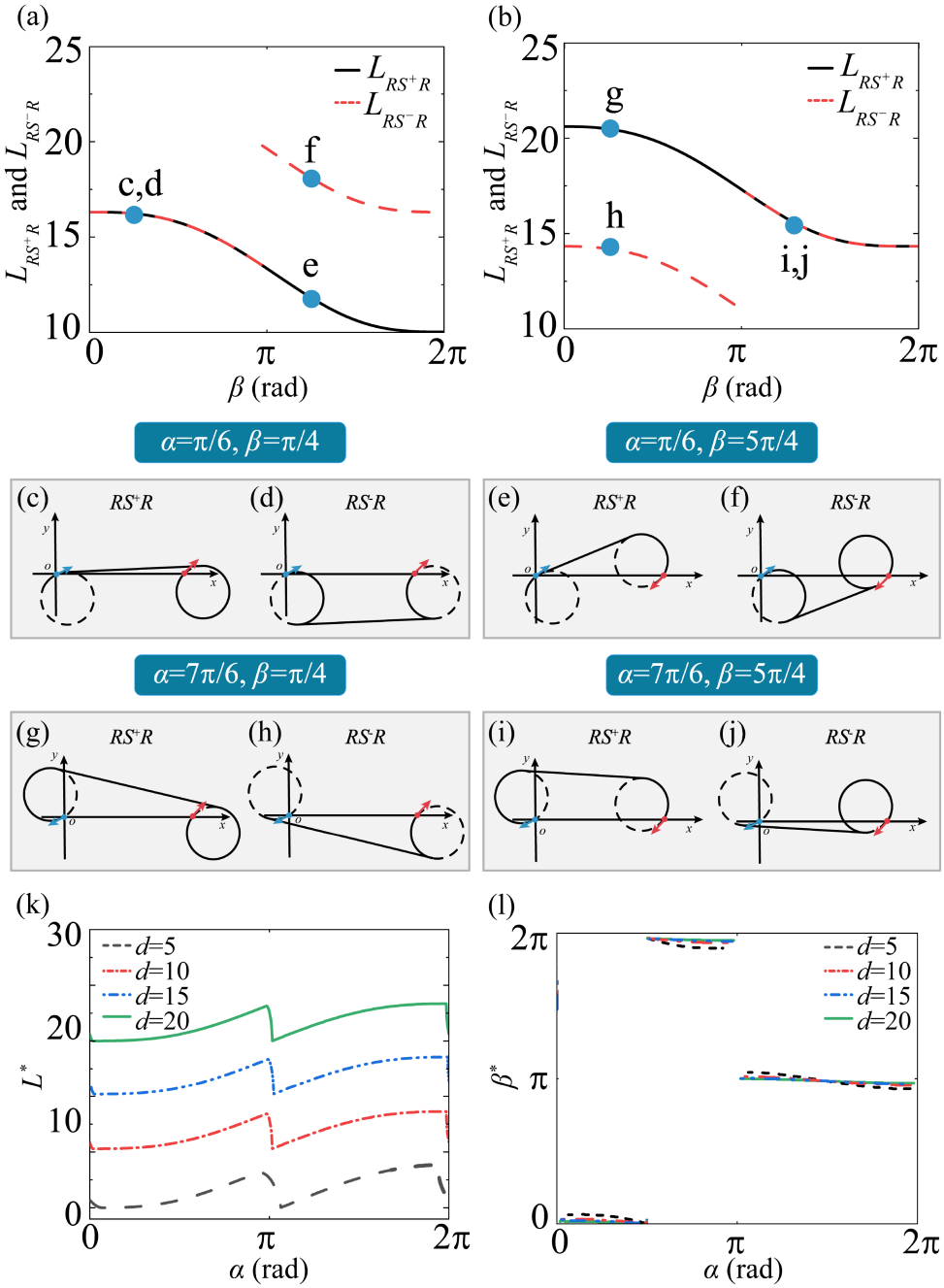

Fig. 3. Optimal value. (a) The optimal value of β when $\alpha = \pi/6$ and $d = 10$. (b) The optimal value of β when $\alpha = 7\pi/6$ and $d = 10$. (c)–(j) The corresponding optimal trajectories for $(\alpha, \beta) = (\pi/6, \pi/4)$, $(\alpha, \beta) = (\pi/6, 5\pi/4)$, $(\alpha, \beta) = (7\pi/6, \pi/4)$, $(\alpha, \beta) = (7\pi/6, 5\pi/4)$. (k) and (l) Optimal value L^* and β^* as a function of α for different d.

There is a critical angle of β_c that distinguishes the optimal path. For $(\alpha, d) = (\pi/6, 10)$, both the RS^+R and RS^-R are optimal paths when $0 \le \beta \le \beta_c$, and only the RS^+R is the optimal path when $\beta_c < \beta \le 2\pi$. For $(\alpha, d) = (7\pi/6, 10)$, only the RS^-R is the optimal path when $0 \le \beta \le \beta_c$, and both RS^+R and RS^-R are optimal paths when $\beta_c < \beta \le 2\pi$. The critical value for $(\alpha, d) = (\pi/6, 10)$ and $(7\pi/6, 10)$ are 3.06 and 3.22, respectively. Fig. 3(c)–(j) shows the corresponding optimal trajectories for $(\alpha, \beta) = (\pi/6, \pi/4)$, $(\pi/6, 5\pi/4)$, $(7\pi/6, \pi/4)$, and $(7\pi/6, 5\pi/4)$, respectively.

The modified Dubins method provides a three-segment optimal path for the electric-driven soft robot with a prescribed destination orientation. In practice, the destination orientation is generally not restricted due to the self-adaptability. When β is not prescribed, the shortest optimal path can be obtained by differentiating the minimum value of L_{RS^+R} and L_{RS^-R} with respect to β. The shortest optimal path L^* and the corresponding β^* are obtained numerically for each pair of (α, d). Fig. 3(k) and (l) plots the dependence of the length of the shortest optimal path L^* and the corresponding β^* on α for various d ranging from 5

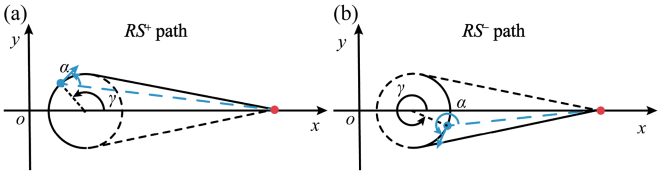

Fig. 4. Two-segment path RS^+ and RS^-. The trajectories of (a) RS^+ path and (b) RS^- path. RS^+ path is preferred when $0 \leq \alpha < \pi$, while RS^- path is preferred when $\pi \leq \alpha < 2\pi$.

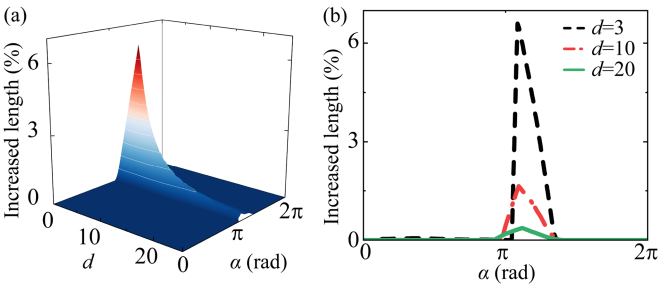

Fig. 5. Increased length of two-segment path. (a) Increased length as a function of d and α. (b) Increased length on α for different d.

to 20. The optimal orientation β^* is found to distribute in three discrete regions: around 0, 2π, and π.

C. Two-Segment Optimal Path

In navigating complex environments or under external disturbances, minimizing the number of path segments simplifies the control of soft robots. For a given pair (α, d), the three-segment optimal path is simplified to a two-segment path consisting of a right turn and a forward or backward path denoted as RS^+ and RS^- [see Fig. 4(a) and (b)]. The RS^+ path is preferred when $0 \leq \alpha < \pi$, while RS^- path is preferred when $\pi \leq \alpha < 2\pi$.

Fig. 5(a) plots the increased path length compared to the shortest three-segment optimal path for different d and α. When d is above 3.6, the increased length of the two-segment path is within 5% of the three-segment shortest optimal path when α ranges from 0 to 2π. Fig. 5(b) plots the increased length as a function of α for different d. The differences are generally small, except when α is near π. The maximum difference increases when d decreases.

IV. Feedback Control

A vision-based feedback method for the real-time adjustment of the optimal path is developed to enhance the accuracy and robustness of the soft robot's locomotion. The experimental setup, control algorithm, and stability analysis of the feedback control of the soft robots are illustrated.

A. Experimental Setup

Vision-based feedback is used to adjust the optimal path in real-time. The approach is an instance of IBVS [47]. Fig. 6(a) illustrates the experiment setup. A camera (MER2-503-36U3C, Daheng Image) captures images of the soft robot at a frame rate of 15 frames per second. These raw images are transmitted

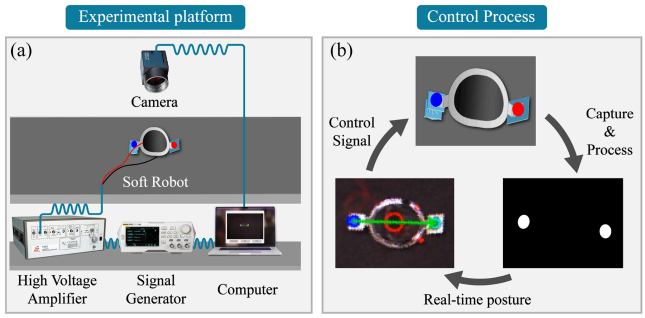

Fig. 6. Setup of the vision-based feedback control. (a) Experimental setup. (b) The laptop processes the raw image by color segmentation based on HSV, provides feedback on the posture, then sends control signals to the soft robot.

to a laptop where color segmentation based on HSV (Hue, Saturation, Value) is used to identify the positions of the soft robot's front and back feet [see Fig. 6(b)]. The vector connecting the front and back feet indicates the orientation of the soft robot. Based on the coordinates and orientations obtained, the modified Dubins path planning is conducted. The control signal is sent to a signal generator (DG822, RIGOL), which produces a programmed sinusoidal wave to a high-voltage amplifier (10/10B-HS, TREK). The high-voltage amplifier amplifies the input signal and outputs a high voltage with varying frequency to control the motions of the soft robots.

B. Control Algorithm

The soft robotic system is a nonlinear time-varying system with discrete inputs. The state variable vector $\mathbf{x}$ of the soft robot can be described as

$$\mathbf{x} = [x, y, \theta]^T \tag{15}$$

where (x, y) describe the normalized position, and θ is the orientation. The dynamics are represented by

$$\dot{x} = u_1 \cos(\theta), \dot{y} = u_1 \sin(\theta), \dot{\theta} = u_2 \tag{16}$$

where u_1 and u_2 are the normalized linear and angular velocities, respectively. Thus, the soft robotic system can be formalized using the state-space description as

$$\dot{\mathbf{x}} = A\mathbf{x} + B\mathbf{u} \tag{17}$$

where

$$\mathbf{u} = [u_1, u_2],\ A = \begin{bmatrix} 0 & 0 & 0 \\ 0 & 0 & 0 \\ 0 & 0 & 0 \end{bmatrix} \text{ and } B = \begin{bmatrix} \cos(\theta) & 0 \\ \sin(\theta) & 0 \\ 0 & 1 \end{bmatrix}. \tag{18}$$

The forward, backward, and angular velocities are measured and normalized by the minimum turning radius. The normalized forward, backward, and angular velocities are 0.37 s^{-1}, 0.41 s^{-1}, and 0.37 rd s^{-1}, respectively. Therefore, the three inputs for the soft robotic system are the forward motion with $\mathbf{u} = [0.37, 0]$, backward motion $\mathbf{u} = [-0.41, 0]$, and right turn $\mathbf{u} = [0.37, 0.37]$.

A straightforward control method is used to ensure the soft robot reaches the target. The soft robot turns right when the

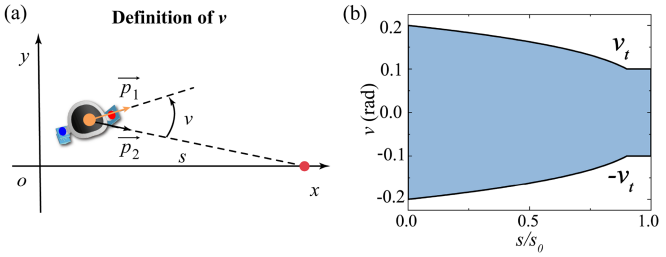

Fig. 7. Control strategy. (a) Definition of the deviation angle v. (b) The dependence of the threshold angle v_t with s/s_0.

TABLE III
PSEUDOCODE OF THE PATH PLANNING ALGORITHM

Algorithm Pseudo-code for the Path Planning Algorithm

1: Define the initial and target points.
2: Establish a new coordinate by setting the origin, the x-axis, and normalization.
3: Calculate the initial state and target position in the new coordinate.
4: **While** target position not reached **do**
5: Capture the image of the soft robot at a frequency of 15 Hz
6: Process the images to calculate the real-time state **x**.
7: Calculate the distance s and deviation angle v from **x**.
8: Calculate the threshold angle v_t.
9: **if** $v > v_t$ **then**
10: The soft robot turns right.
11: **else if** $v < -v_t$ **then**
12: The soft robot goes backward.
13: **else**
14: The soft robot goes forward.
15: **end if**
16: **end while**

deviation angle $v > v_t$, goes straight when $|v| \leq v_t$, and moves backward when $v < -v_t$. The deviation angle v is the angle between the orientation of the soft robot $\vec{p}_1$ and the direction to the target $\vec{p}_2$ [see Fig. 7(a)]. The threshold v_t is defined to avoid frequent changes in the inputs. v_t changes with distances and is given by

$$v_t = \begin{cases} 0.1, & \text{when } 0.9 < \frac{s}{s_0} \leq 1 \\ 0.2\left[\frac{(s_0-s)}{s_0}\right]^{\frac{\ln(2)}{\ln(10)}}, & \text{when } 0 \leq \frac{s}{s_0} \leq 0.9. \end{cases} \quad (19)$$

The second form is derived by fitting an exponential function $y = (1-x)^n$ with boundary conditions $v_t = 0.2$ at $s/s_0 = 0$ and $v_t = 0.1$ at $s/s_0 = 0.9$ to ensure smoothness of the threshold curve. Fig. 7(b) plots the dependence of v_t on s/s_0. Table III shows the pseudocode of the path-planning algorithm.

C. Stability Analysis

Given the nonlinear and time-varying nature of the soft robotic system, stability is evaluated numerically using MATLAB by introducing random noises to the state variables x, y, and θ at each step

$$\begin{aligned} x_{t+\Delta t} &= x_t + \dot{x}_t \Delta t + \varepsilon \\ y_{t+\Delta t} &= y_t + \dot{y}_t \Delta t + \varepsilon \\ \text{and} \quad \theta_{t+\Delta t} &= \theta_t + \dot{\theta}_t \Delta t + \varepsilon. \end{aligned} \quad (20)$$

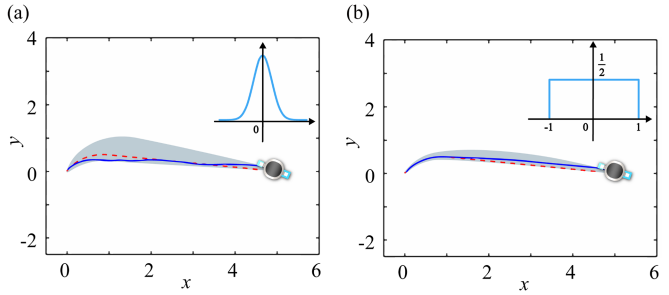

Fig. 8. Simulated trajectories of the soft robots under (a) Gaussian and (b) uniform noise distribution with an amplitude of 0.01.

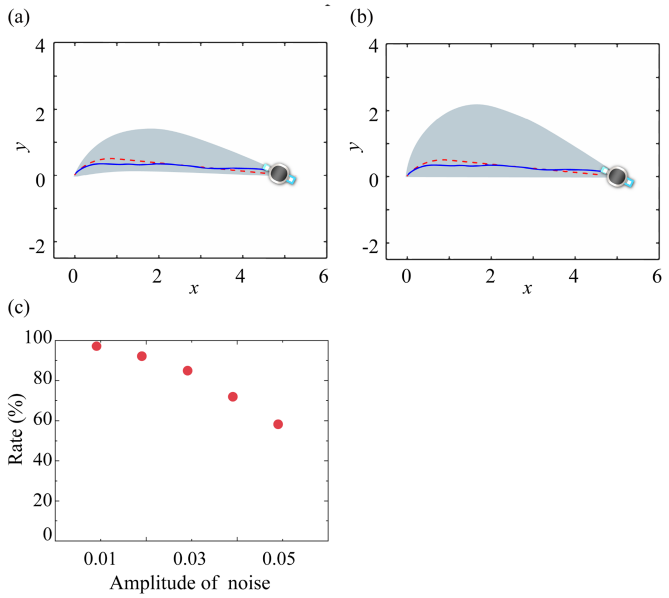

Fig. 9. Trajectories under Gaussian noise with an amplitude of (a) 0.02 and (b) 0.03. (c) Rates of reaching the target position with varying noise amplitudes.

Δt is the duration of each time step. The subscripts t and $t+\Delta t$ represent the states at the current and next steps, respectively. $\dot{x}_t = u_1 \cos\theta_t$, $\dot{y}_t = u_1 \sin\theta_t$, and $\dot{\theta}_t = u_2$ from (16). The input $[u_1, u_2]$ are [0.37, 0], [−0.41, 0], or [0.37, 0.37] for forward, backward, and right-turn motions, respectively. The term ε represents the applied noise. Both Gaussian and uniform noise distributions are used in the simulation. Gaussian noise follows a standard Gaussian distribution, while uniform noise follows a uniform distribution over the interval [-1, 1]. In the numerical simulation, $\Delta t = 1/15s$. Thus, the maximum state variable change

$$\begin{aligned} &\max\left(|\dot{x}_t \Delta t|, |\dot{y}_t \Delta t|, \left|\dot{\theta}_t \Delta t\right|\right) \\ &= \max\left(|u_1 \cos\theta_t \Delta t|, |u_1 \sin\theta_t \Delta t|, |u_2 \Delta t|\right) \\ &\leq \max\left(|u_1 \Delta t|, |u_2 \Delta t|\right) = 0.027. \end{aligned} \quad (21)$$

Fig. 8(a) and (b) shows the simulated trajectories of the soft robots under Gaussian and uniform noise distribution, respectively. The amplitude of ε is set to 0.01, comparable to the maximum state variable change of 0.027. A total of

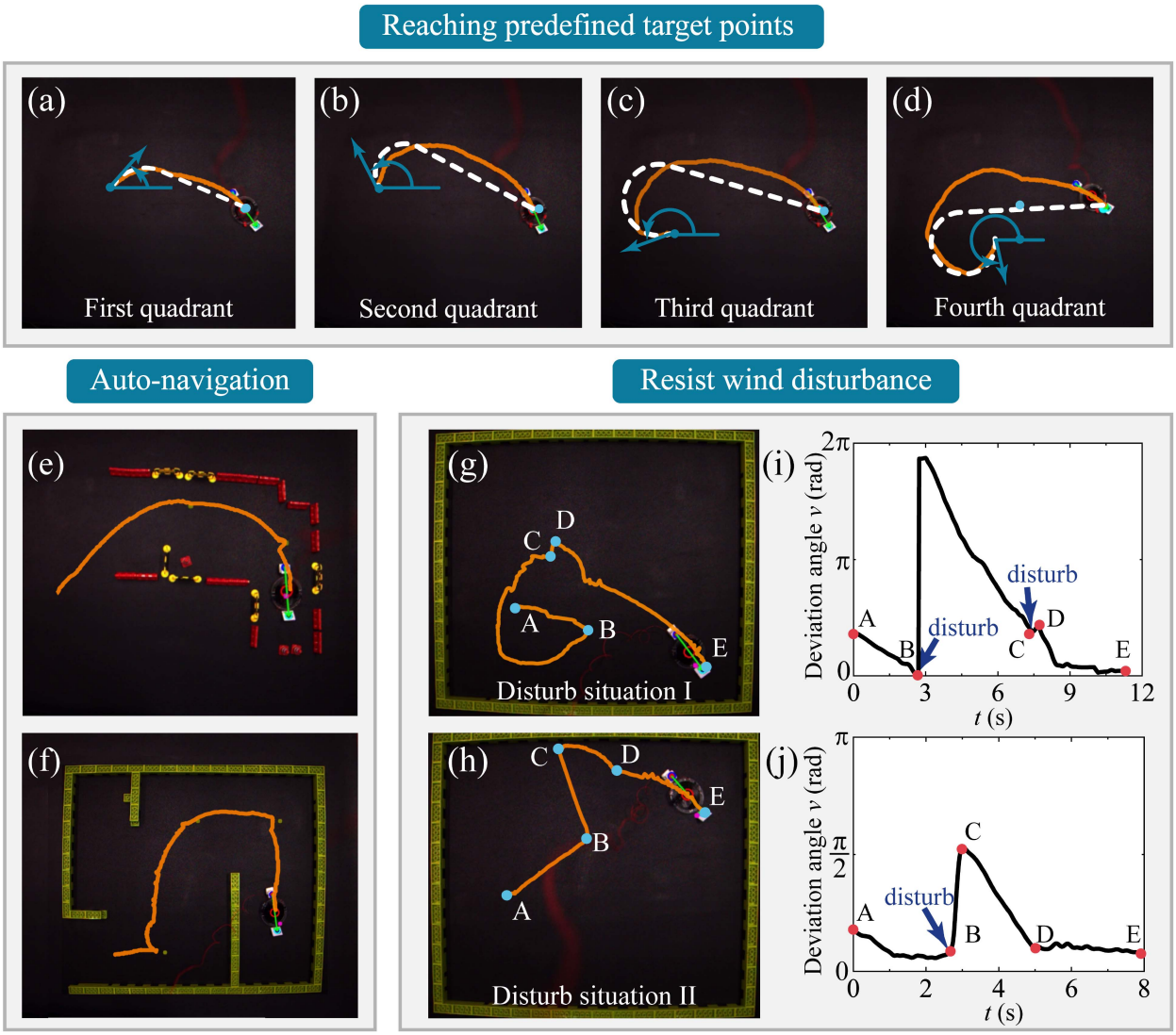

Fig. 10. Experimental demonstrations. (a)–(d) Autonomous reaching of predefined target points from varying initial orientations spanning all four quadrants. (e) and (f) Soft robot navigating mazes autonomously by avoiding obstacles. (g) and (h) Soft robot resisting wind disturbances by restoring the optimized trajectory. (i) and (j) Dependences of the deviation angle v on time t.

5000 simulations were run for each type of noise to capture the stability behaviors. The red curve represents the theoretical trajectories without noise, and the blue curve represents a typical trajectory under noise. The gray region indicates the domain of trajectories that reach the target. The rates of reaching the target are 97.06% with Gaussian noise and 99.90% with uniform noise, demonstrating the system's robustness.

To further explore the effect of the noise amplitude, the stability analysis under Gaussian noises with different amplitudes ranging from 0.01 to 0.05 was conducted. Typical trajectories and domains with amplitude of 0.02 and 0.03 are shown in Fig. 9(a) and (b). It can be seen that the areas of trajectory domains increase with the noise amplitude. The rates of reaching the target positions are 97.06%, 92.12%, 84.88%, 72.02%, and 58.28% as the amplitude changes from 0.01 to 0.05 [see Fig. 9(c)]. Note that the chosen amplitudes are significant compared to the maximum state variable change of 0.027.

V. Experimental Demonstrations

This section presents the implementation of the modified Dubins path planning with vision-based feedback control on electric-driven soft robots. Demonstrations include reaching points with different initial orientations, navigating mazes, and reaching destinations under wind disturbances.

A. Reaching Points With Different Initial Orientations

The capability of the soft robots to autonomously reach target points from various initial orientations is demonstrated, as illustrated in Movie 2. The initial and target positions are fixed, while the initial orientations of the soft robot span all four quadrants. Fig. 10(a)–10(d) shows the trajectories of the soft robot for these four different cases. All trajectories closely match the theoretical two-segment optimal paths, with minor discrepancies due to the unstable locomotion of the soft robots. Following the modified

Dubins path, the soft robots consistently reach the target points regardless of their initial orientation and unstable locomotion.

B. Autonomous Maze Navigation

Next, the soft robots' ability to navigate mazes autonomously is evaluated (Movie 3 and 4). Given the presence of obstacles, several intermediate target points are manually chosen to facilitate navigation toward the ultimate destination. Two different maze configurations are used. Fig. 10(e) and (f) depicts the trajectories of the soft robots within the maze. The yellow points indicate the intermediate target points. The soft robots successfully reach each intermediate target point and ultimately the destination. Despite notable deviations from the optimal path due to large drag forces generated by the conductive wire, the proposed feedback control algorithm adjusts trajectories in real time, ensuring arrival at the destination.

C. Locomotion Under Wind Disturbance

To further validate the effectiveness of the control algorithm, external wind disturbances is applied during locomotion (Movie 5). An air blower is employed to generate substantial wind disturbances. Two different scenarios are shown in Fig. 10(g) and (h). In the first scenario [see Fig. 10(g)], the soft robot starts at point A and aims to reach point E. Initially, it moves from point A to B. At point B, it encounters wind disturbances, significantly altering its orientation due to its lightweight nature. Fig. 10(i) shows the deviation angle v over time t, where the orientation angle changes around 350° at point B. The soft robot then restores its desired orientation by turning right, following the two-segment optimal path. Another wind disturbance occurs at point C, shifting the robot to point D. Ultimately, the soft robot reaches point E after real-time adjustments to its path.

In the second scenario [see Fig. 10(h)], the soft robot initially follows the RS^{+} path from point A to B. A disturbance causes a discrepancy from point B to C. Subsequently, the soft robot corrects its trajectory and moves from point C to D, finally reaching point E. The trajectory and deviation angle v over time t are shown in Fig. 10(h) and (j). Despite significant positional and orientational deviations due to disturbances, the soft robot promptly adjusts its path in real time, successfully reaching the destinations.

VI. Conclusion

Controlling DE is crucial for stable locomotion due to the inherent viscoelastic nonlinearity. Extensive research has been conducted on material characterization, modeling, and implementation of DE control strategies. For example, Rizzello et al. [51] developed a sensorless control algorithm for DE-based positioning systems, a model-based control strategy for bistable positioning systems to enhance stability and performance across operational ranges [52], and a feedforward control strategy tailored for micropositioning applications [53]. These studies aim for precise and efficient DE operations. Other than the specific motion control of the DE actuator, this work uses structural design to generate multimodal motions and studies the path planning control of the soft robots as a whole.

The size of the soft robots also affects their locomotion. Experiments were conducted on DE soft robots of different sizes, and their behaviors were analyzed (Movie 6). Soft robots at 0.8 and 1.5 times the original sizes were fabricated. Scaling the soft robots necessitates adjustments in design parameters, particularly the thickness of the acrylic frame. A thick frame causes the saddle shape to become too flat to generate sufficient actuation, while a thin frame forms a saddle shape with large curvatures, leading to self-contact and potential burning of the soft robot. For example, the 0.8-sized soft robot with a thicker frame demonstrated restricted forward motion. For the 1.5-size soft robot, two different thicknesses (0.4 mm and 0.5 mm) were tested. The thinner frame (0.4 mm) led to DEA self-contact and consequent burning upon actuation, while the thicker frame (0.5 mm) limited the soft robot to only forward motion. Therefore, design parameters should be carefully chosen to enable all three motion modes. If the scaled soft robots exhibit all three motions, the path planning method can be adapted and implemented across DE soft robots, as the control method is independent of the size of the soft robots.

Further research is necessary to realize practical applications, including structural design, theoretical modeling, high-resolution fabrication and the integration of advanced algorithms. Currently, the capacity for multimodal motion in soft robots is limited. Structural design can incorporate embedded intelligence into the soft robots' physical structure, enhancing their multimodal capabilities. In this work, we utilized the dynamic behaviors of a chiral lattice to achieve multimodal motion from a single voltage input. Yet, these robots are limited to three movements: forward, backward, and turning right, with feedback control managed by an external camera. By integrating the structural design of metamaterials and the stimuli-feedback of active materials, multimodal motions and integrated actuation and sensing can be enhanced.

Moreover, accurate control of the soft robots requires the development of theoretical modeling. Soft materials exhibit an infinite degree of freedom and material nonlinearity. Models that capture these nonlinear behaviors are crucial for predicting deformation and motion, enabling their integration into feedback control algorithms for precise maneuvering. High-resolution fabrication techniques are also critical for ensuring consistent motion under actuation and facilitating precise control. Due to the use of soft materials, traditional fabrication methods for rigid materials are unsuitable for soft robots. 3-D printing is a promising fabrication method for the multifunctional and multimaterial demands of soft robots. Advancements in multimaterial 3-D printing technologies, the development of printable soft materials, and the simulation of the printing process are imperative for progress in this area.

Last, the practical application of soft robots further requires the integration of advanced control algorithms. Soft robots are designed to work in unstructured and dynamically changing environments. Machine learning, such as, reinforcement learning, allows soft robots to learn from interaction with the environment, continuously improving their performance as they encounter new situations, obstacles, or tasks. This adaptability is crucial for applications such as, search and rescue, underwater exploration, and interaction with humans or delicate objects.

We have developed a vision-based path planning method for a DE soft robot. Unlike the traditional Dubins method, which considers forward, right and left turn motions, we have modified the Dubins path planning algorithm to account for the forward, backward, and right turn motions of the soft robots. We further demonstrate that the three-segment optimal path can be reduced to a two-segment path with negligible length increments, facilitating the implementation of the algorithm in soft robots. IBVS is used for real-time adjustments of the locomotion path. Experiments demonstrate the ability of the soft robots to reach points with different initial orientations, navigate mazes, and reach destinations despite wind disturbances.

REFERENCES

[1] S. Y. Hann, H. Cui, M. Nowicki, and L. G. Zhang, "4D printing soft robotics for biomedical applications," *Additive Manuf.*, vol. 36, 2020, Art. no. 101567.

[2] B. Mazzolai et al., "Roadmap on soft robotics: Multifunctionality, adaptability and growth without borders," *Multifunctional Mater.*, vol. 5, no. 3, 2022, Art. no. 032001.

[3] E. Roels et al., "Processing of self-healing polymers for soft robotics," *Adv. Mater.*, vol. 34, no. 1, 2022, Art. no. 2104798.

[4] E. S. Keneth, A. Kamyshny, M. Totaro, L. Beccai, and S. Magdassi, "3D printing materials for soft robotics," *Adv. Mater.*, vol. 33, no. 19, 2021, Art. no. 2003387.

[5] D. Wang et al., "Soft actuators and robots enabled by additive manufacturing," *Annu. Rev. Control, Robot., Auton. Syst.*, vol. 6, pp. 31–63, 2023.

[6] D. Drotman, S. Jadhav, D. Sharp, C. Chan, and M. T. Tolley, "Electronics-free pneumatic circuits for controlling soft-legged robots," *Sci. Robot.*, vol. 6, no. 51, 2021, Art. no. eaay2627.

[7] N. Vasios, A. J. Gross, S. Soifer, J. T. Overvelde, and K. Bertoldi, "Harnessing viscous flow to simplify the actuation of fluidic soft robots," *Soft Robot.*, vol. 7, no. 1, pp. 1–9, 2020.

[8] F. Connolly, C. J. Walsh, and K. Bertoldi, "Automatic design of fiber-reinforced soft actuators for trajectory matching," *Proc. Nat. Acad. Sci.*, vol. 114, no. 1, pp. 51–56, 2017.

[9] C. Jiang, D. Wang, B. Zhao, Z. Liao, and G. Gu, "Modeling and inverse design of bio-inspired multi-segment pneu-net soft manipulators for 3D trajectory motion," *Appl. Phys. Rev.*, vol. 8, no. 4, p. 041416, 2021, doi: 10.1063/5.0054468.

[10] L. Jin, A. E. Forte, B. Deng, A. Rafsanjani, and K. Bertoldi, "Kirigami-inspired inflatables with programmable shapes," *Adv. Mater.*, vol. 32, no. 33, 2020, Art. no. 2001863.

[11] D. Wang, C. Jiang, and G. Gu, "Modeling and design of lattice-reinforced pneumatic soft robots," *IEEE Trans. Robot.*, vol. 40, pp. 606–623, 2024.

[12] Y. Cheng et al., "A fast autonomous healing magnetic elastomer for instantly recoverable, modularly programmable, and thermorecyclable soft robots," *Adv. Funct. Mater.*, vol. 31, no. 32, 2021, Art. no. 2101825.

[13] Y. Dong et al., "Untethered small-scale magnetic soft robot with programmable magnetization and integrated multifunctional modules," *Sci. Adv.*, vol. 8, no. 25, 2022, Art. no. eabn8932.

[14] N. Ebrahimi et al., "Magnetic actuation methods in bio/soft robotics," *Adv. Funct. Mater.*, vol. 31, no. 11, 2021, Art. no. 2005137.

[15] J. Wang, D. Wang, L. Dong, M. Zhang, and G. Gu, "Analytical modeling and inverse design of centimeter-scale hard-magnetic soft robots," *IEEE Trans. Automat. Sci. Eng.*, early access, Sep. 18, 2023, doi: 10.1109/TASE.2023.3313395.

[16] R. Zhao, H. Dai, and H. Yao, "Liquid-metal magnetic soft robot with reprogrammable magnetization and stiffness," *IEEE Robot. Automat. Lett.*, vol. 7, no. 2, pp. 4535–4541, Apr. 2022.

[17] M. Duduta, D. R. Clarke, and R. J. Wood, "A high speed soft robot based on dielectric elastomer actuators," in *Proc. 2017 IEEE Int. Conf. Robot. Automat. IEEE, Conf. Proc.*, 2017, pp. 4346–4351.

[18] X. Ji et al., "An autonomous untethered fast soft robotic insect driven by low-voltage dielectric elastomer actuators," *Sci. Robot.*, vol. 4, no. 37, 2019, Art. no. eaaz6451.

[19] W.-B. Li, W.-M. Zhang, H.-X. Zou, Z.-K. Peng, and G. Meng, "A fast rolling soft robot driven by dielectric elastomer," *IEEE/ASME Trans. Mechatron.*, vol. 23, no. 4, pp. 1630–1640, Aug. 2018.

[20] Z. Ren et al., "A high-lift micro-aerial-robot powered by low-voltage and long-endurance dielectric elastomer actuators," *Adv. Mater.*, vol. 34, no. 7, 2022, Art. no. 2106757.

[21] S. I. Rich, R. J. Wood, and C. Majidi, "Untethered soft robotics," *Nature Electron.*, vol. 1, no. 2, pp. 102–112, 2018.

[22] G. Rizzello, P. Serafino, D. Naso, and S. Seelecke, "Towards sensorless soft robotics: Self-sensing stiffness control of dielectric elastomer actuators," *IEEE Trans. Robot.*, vol. 36, no. 1, pp. 174–188, Feb. 2020.

[23] J. Shintake, V. Cacucciolo, H. Shea, and D. Floreano, "Soft biomimetic fish robot made of dielectric elastomer actuators," *Soft Robot.*, vol. 5, no. 4, pp. 466–474, 2018.

[24] Q. Ren, W. Zhu, J. Cao, and W. Liang, "Neuro-inspired motion control of a soft myriapod robot," *IEEE Trans. Cogn. Devlop. Syst.*, vol. 16, no. 2, pp. 606–617, Apr. 2024.

[25] A. T. Khan, S. Li, S. Kadry, and Y. Nam, "Control framework for trajectory planning of soft manipulator using optimized RRT algorithm," *IEEE Access*, vol. 8, pp. 171730–171743, 2020. [Online]. Available: https://ieeexplore.ieee.org/ielx7/6287639/8948470/09199815.pdf?tp=&arnumber=9199815&isnumber=8948470&ref=

[26] A. D. Marchese, R. K. Katzschmann, and D. Rus, "Whole arm planning for a soft and highly compliant 2D robotic manipulator," in *Proc. 2014 IEEE/RSJ Int. Conf. Intell. Robots Syst., Conf. Proc.*, 2014, pp. 554–560. [Online]. Available: https://ieeexplore.ieee.org/document/6942614/

[27] J. Lai, B. Lu, Q. Zhao, and H. K. Chu, "Constrained motion planning of a cable-driven soft robot with compressible curvature modeling," *IEEE Robot. Automat. Lett.*, vol. 7, no. 2, pp. 4813–4820, Apr. 2022. [Online]. Available: https://ieeexplore.ieee.org/document/9716747/

[28] H. Liu, Y. Jiang, M. Liu, X. Zhang, J. Huo, and H. Su, "Path planning with obstacle avoidance for soft robots based on improved particle swarm optimization algorithm," *Intell. Robot.*, vol. 3, no. 4, pp. 565–580, 2023, doi: 10.20517/ir.2023.31. [Online]. Available: https://f.oaes.cc/xmlpdf/c05c5717-1cec-4f3b-ac89-38b2a1b9e877/ir3031.pdf

[29] P. R. Fairchild, V. Srivastava, and X. Tan, "Efficient path planning of soft robotic arms in the presence of obstacles," *IFAC-PapersOnLine*, vol. 54, no. 20, pp. 586–591, 2021.

[30] E. Gough, A. T. Conn, and J. Rossiter, "Planning for a tight squeeze: Navigation of morphing soft robots in congested environments," *IEEE Robot. Automat. Lett.*, vol. 6, no. 3, pp. 4752–4757, Jul. 2021.

[31] H. Wang, J. Chen, H. Y. Lau, and H. Ren, "Motion planning based on learning from demonstration for multiple-segment flexible soft robots actuated by electroactive polymers," *IEEE Robot. Automat. Lett.*, vol. 1, no. 1, pp. 391–398, Jan. 2016.

[32] M. Luo et al., "Motion planning and iterative learning control of a modular soft robotic snake," *Front. Robot. AI*, vol. 7, 2020, Art. no. 599242. [Online]. Available: https://www.frontiersin.org/articles/10.3389/frobt.2020.599242

[33] A. Askari, M. Mortazavi, H. Talebi, and A. Motamedi, "A new approach in UAV path planning using bezier-dubins continuous curvature path," *Proc. Inst. Mech. Engineers, Part G: J. Aerosp. Eng.*, vol. 230, no. 6, pp. 1103–1113, 2016.

[34] X. Du, X. Li, D. Liu, and B. Dai, "Path planning for autonomous vehicles in complicated environments," in *Proc. 2016 IEEE Int. Conf. Veh. Electron. Saf., Conf. Proc.*, 2016, pp. 1–7.

[35] M. Owen, R. W. Beard, and T. W. McLain, "Implementing dubins airplane paths on fixed-wing UAVs*," in *Handbook of Unmanned Aerial Vehicles*, K. P. Valavanis and G. J. Vachtsevanos, Eds., Dordrecht, Netherlands: Springer Netherlands, 2015, pp. 1677–1701.

[36] P. Váňa and J. Faigl, "Optimal solution of the generalized dubins interval problem: Finding the shortest curvature-constrained path through a set of regions," *Auton. Robots*, vol. 44, no. 7, pp. 1359–1376, 2020, doi: 10.1007/s10514-020-09932-x.

[37] I. Lugo-Cárdenas, G. Flores, S. Salazar, and R. Lozano, "Dubins path generation for a fixed wing UAV," in *Proc. 2014 Int. Conf. Unmanned Aircr. Syst.*, 2014, pp. 339–346.

[38] M. A. A. Hemmat, Z. Liu, and Y. Zhang, "Real-time path planning and following for nonholonomic unmanned ground vehicles," in *Proc. 2017 Int. Conf. Adv. Mechatron. Syst.*, 2017, pp. 202–207.

[39] P. Maini and P. Sujit, "Path planning for a UAV with kinematic constraints in the presence of polygonal obstacles," in *Proc. 2016 Int. Conf. Unmanned Aircr. Syst.*, 2016, pp. 62–67.

[40] Y. Lin and S. Saripalli, "Path planning using 3D dubins curve for unmanned aerial vehicles," in *Proc. 2014 Int. Conf. Unmanned Aircr. Syst.*, 2014, pp. 296–304.

[41] Y. Kuwata, J. Teo, G. Fiore, S. Karaman, E. Frazzoli, and J. P. How, "Real-time motion planning with applications to autonomous urban driving," *IEEE Trans. Control Syst. Technol.*, vol. 17, no. 5, pp. 1105–1118, Sep. 2009.

[42] X. Song and S. Hu, "2D path planning with dubins-path-based A* algorithm for a fixed-wing UAV," in *Proc. 2017 3rd IEEE Int. Conf. Control Sci. Syst. Eng.*, 2017, pp. 69–73.
[43] H. Min, X. Xiong, P. Wang, and Y. Yu, "Autonomous driving path planning algorithm based on improved A* algorithm in unstructured environment," *Proc. Inst. Mech. Engineers, Part D: J. Automobile Eng.*, vol. 235, no. 2/3, pp. 513–526, 2021.
[44] X. Ma and D. A. Castanon, "Receding horizon planning for dubins traveling salesman problems," in *Proc. 45th IEEE Conf. Decis. Control, Conf. Proc.*, 2006, pp. 5453–5458.
[45] H. J. Choi, "Time-optimal paths for a dubins car and dubins airplane with a unidirectional turning constraint," Master's Thesis, 2014.
[46] D. Wang et al., "Dexterous electrical-driven soft robots with reconfigurable chiral-lattice foot design," *Nature Commun.*, vol. 14, no. 1, 2023, Art. no. 5067.
[47] A. C. Sanderson and L. E. Weiss, *Adaptive Visual Servo Control of Robots*. Berlin, Germany: Springer, 1983, pp. 107–116.
[48] F. Xu, H. Wang, W. Chen, and Y. Miao, "Visual servoing of a cable-driven soft robot manipulator with shape feature," *IEEE Robot. Automat. Lett.*, vol. 6, no. 3, pp. 4281–4288, Jul. 2021.
[49] J. F. Lazo et al., "Autonomous intraluminal navigation of a soft robot using deep-learning-based visual servoing," in *Proc. 2022 IEEE/RSJ Int. Conf. Intell. Robots Syst.*, 2022, pp. 6952–6959.
[50] L. E. Dubins, "On curves of minimal length with a constraint on average curvature, and with prescribed initial and terminal positions and tangents," *Amer. J. Math.*, vol. 79, no. 3, pp. 497–516, 1957.
[51] G. Rizzello, D. Naso, A. York, and S. Seelecke, "Closed loop control of dielectric elastomer actuators based on self-sensing displacement feedback," *Smart Mater. Structures*, vol. 25, no. 3, 2016, Art. no. 035034.
[52] G. Rizzello, D. Naso, B. Turchiano, and S. Seelecke, "Robust position control of dielectric elastomer actuators based on LMI optimization," *IEEE Trans. Control Syst. Technol.*, vol. 24, no. 6, pp. 1909–1921, Nov. 2016.
[53] S. Hau, G. Rizzello, M. Hodgins, A. York, and S. Seelecke, "Design and control of a high-speed positioning system based on dielectric elastomer membrane actuators," *IEEE/ASME Trans. Mechatron.*, vol. 22, no. 3, pp. 1259–1267, Jul. 2017.

Xinlei Li received the B.Eng degree in mechanical engineering from Shanghai Jiao Tong University, China, in 2022. She is currently working toward the master degree in mechanical engineering with the Shanghai Jiao Tong University, China.

Her research interests include 4-D printing and soft robotics, especially the modeling and design of dielectric elastomer robot.

Dong Wang received the B.Eng degree in mechanical engineering from Zhejiang University, China, in 2010, and the Ph.D. degree in mechanical engineering from Nanyang Technology University, Singapore, in 2015.

He is currently working as an Associate Professor with the School of Mechanical Engineering, Shanghai Jiao Tong University, China. His research interests include 4-D printing and soft robotics.